Biointerface Research in Applied Chemistry
Open-Access Journal (ISSN: 2069-5837)

Article
Volume 16, Issue 2, 2026, 56
https://doi.org/10.33263/BRIAC162.056

Exploring the Therapeutic Potential of Barley β-Glucan in Lung Cancer: An *In vitro* and *In silico* Investigation

Rohan Kumar [1], Adil Ali [1], Tarun Kumar Upadhyay [1,*]

[1] Department of Biotechnology, Parul Institute of Applied Sciences and Research and Development Cell, Parul University, Vadodara 391760, Gujarat-India
* Correspondence: tarun.upadhyay35971@paruluniversity.ac.in;

Received: 2.07.2025; Accepted: 19.01.2026; Published: 15.04.2026

Abstract: Lung cancer (LC) remains a major cause of cancer-related deaths worldwide. In this study, we explored how barley β-glucan (BBG) inhibits lung cancer cells (A549) using *in vitro* experiments and computer-based modeling to evaluate its therapeutic and antioxidant properties. This research is unique in its focus on β-glucan derived from cereal grains, an area that has received less attention compared to β-glucan from other sources. The structure of the extracted BBG was confirmed using FTIR and UV–vis spectroscopy techniques. Several antioxidant tests, including DPPH and FRAP assays, as well as other radical-scavenging methods, demonstrated that BBG effectively neutralizes free radicals. Computer simulations, such as molecular docking and PPI mapping, indicated that BBG binds strongly to key proteins involved in cancer development. *In vitro* tests on A549 cells showed significant cell death and increased reactive oxygen species production, while BBG exhibited minimal cytotoxicity to healthy L929 cells and almost no toxicity to RBCs. These findings suggest that BBG has considerable potential as a natural compound with both antioxidant and anticancer properties, making it a promising candidate for future therapeutic applications in LC treatment.

Keywords: anticancer; antioxidant; barley β-glucan; molecular docking; network pharmacology; apoptosis.

1. Introduction

Lung cancer (LC) is a cause of cancer morbidity and mortality worldwide, accounting for a substantial proportion of cancer diagnoses and deaths, nearly one in eight (12.4%) and one in five (18.7%), respectively, in 2022 [1]. In terms of incidence and mortality, LC ranks highest among males and comparatively lower among females, with significant regional variations. Tobacco use remains the predominant etiological factor. Among histological subtypes, adenocarcinoma has emerged as the most prevalent form globally, surpassing squamous cell carcinoma (SCC) in both men and women [1].

β-glucans (BG) are major structural polysaccharides present in the cell walls of microorganisms such as yeast and mushrooms, as well as in cereals like oats and barley. They are glucose polymers connected through β-(1,3)-glycosidic linkages with species-specific side branches, primarily β-(1,4) or β-(1,6), that determine their biological activity [2,3]. Barley-derived β-glucan (BBG) contains mixed (1,3) and (1,4) β-D-glucopyranose linkages, contributing to its solubility and distinctive functional properties [4,5]. Previous research has

shown that BBG can regulate blood cholesterol and glucose levels, reduce visceral fat, and exert cardiovascular benefits [6].

While β-glucans from non-cereal sources such as fungi and yeast have been widely investigated for their immunomodulatory and anticancer properties [7], cereal-derived β-glucans, particularly those from barley, remain underexplored in oncology. Given their unique structural linkages, BBGs may interact differently with cellular receptors, thereby modulating oxidative stress and influencing apoptosis in cancer cells. Existing LC treatments, such as surgery, chemotherapy, radiotherapy, and immunotherapy, although effective, are often associated with severe side effects and limited selectivity, underscoring the need for safer and natural therapeutic alternatives [8].

Despite emerging evidence of BBG's therapeutic potential, studies delineating its molecular mechanisms, pharmacokinetic behavior, and cytotoxic selectivity against LC are limited [9–12]. This research, therefore, aimed to investigate the antioxidant, anticancer, and hemocompatibility potential of extracted BBG against lung cancer (A549) and normal (L929) cell lines through *in vitro* and *in silico* analyses. The study also hypothesizes that the mixed β-(1,3)/(1,4) glycosidic linkages of BBG contribute to its anticancer efficacy by modulating redox balance and interacting with key molecular targets involved in LC progression.

2. Materials and Methods

2.1. Reagents and chemicals.

Anthrone reagent, DPPH (2, 2-Diphenyl-1-picrylhydrazyl), sulphuric acid, sodium carbonate, hydrochloric acid, ferric chloride, TPTZ, sodium acetate, potassium persulphate ($K_2S_2O_8$), ABTS (2,2-Azino-bis (3-ethylbenzothiazoline-6 sulfonic acid), hydrogen peroxide, sodium phosphate dibasic, ascorbic acid, potassium phosphate monobasic (KH_2PO_4), acridine orange, and ethidium bromide were purchased from HiMedia. MTT, Hoechst, DCFDA, and propidium iodide dye (Invitrogen) were purchased from Thermo Fisher Scientific.

2.2. Cell culture and maintenance.

Human lung adenocarcinoma (A549) and healthy fibroblast L929 cells were purchased from the National Centre for Cell Science (NCCS, Pune, India). Cells were cultured in DMEM supplemented with 10% FBS and 1% antibiotic-antimycotic solution (Gibco™ Thermo Fisher Scientific) at 37°C in a humidified incubator with 5% CO_2.

2.3. In-silico analysis of barley β-glucan.

2.3.1. ADME properties of β-glucan.

The pharmacokinetic profile of BBG was predicted using pkCSM (https://biosig.lab.uq.edu.au/pkcsm/prediction) [13] and SwissADME pharmacokinetics (http://www.swissadme.ch/index.php#1) [14], which evaluates drug-likeness and ADME characteristics.

2.3.2. ProTox-3.0-prediction of toxicity.

ProTox-3.0- Prediction of Toxicity of Chemicals (https://tox.charite.de/protox3/index.php?site=home) [15] was employed to assess the toxicity

prediction of BBG. ProTox 3.0 employs molecular similarity and machine learning models for assessing acute, organ, and clinical toxicity.

2.3.3. Target prediction.

Using the SwissTargetPrediction database (http://www.swisstargetprediction.ch/), [16,17] potential candidates of BBG were retrieved. Briefly, the BBG canonical smile was obtained from the PubChem database (https://pubchem.ncbi.nlm.nih.gov/) and imported, and match targets were obtained and saved in a CSV file format.

2.3.4. Candidate target collection.

Lung cancer-related targets were retrieved from the GeneCard database (https://www.genecards.org/) [18] and compiled in Excel format for comparative analysis.

2.3.5. Venny 2.1.0.

Venny 2.1.0 database (https://bioinfogp.cnb.csic.es/tools/venny/) was used to identify common targets between BBG and LC through a Venn diagram analysis.

2.3.6. Protein-protein interaction (PPI) network.

String database version 12.0 (https://string-db.org/) [19] was used to construct the PPI network, which was then visualized and refined in Cytoscape 3.10.2 software via the STRING. plug-in

2.3.7. C-T-P network construction.

Cytoscape 3.10.2 software [20]. To study the association between BBG and GeneCard targets, a C-T-P network was constructed using Cytoscape 3.10.2 software with plug-in (CytoNCA), and the corresponding nodes were ranked according to the degree values, and targets with degree> 8 were selected for downstream analysis.

2.3.8. Molecular docking.

Top targets (e.g., CDK1) were obtained from the Protein Data Bank database (https://www.rcsb.org/) [21]. The 3D structure of BBG was downloaded from PubChem (https://pubchem.ncbi.nlm.nih.gov/). Molecular docking was performed with AutoDockTool-1.5.7. The protein structures were prepared by adding polar hydrogens and Kollman charges. The ligand was imported, purified, and both were saved in PDBQT format. Active sites were identified by CASTp 3.0 (http://sts.bioe.uic.edu/castp/index.html?3igg) [22], and a GRID box was generated accordingly. The resulting docked complexes were saved in PDB format and visualized in Discovery Studio Visualizer V21.1.0.20298 (BIOVIA) [23].

2.3.9. BIOVIA (Discovery Studio client 2021).

Discovery Studio Visualizer V21.1.0.20298 (BIOVIA) was used for protein ligand interaction visualization and for generating 2D/3D publication-quality figures.

2.4. β-glucan extraction from barley.

BG extraction using the previously described protocol [24]. Deactivation of barley flour was done at 80°C with 75% EtOH. 20g deactivated barley flour was mixed with 200mL of distilled water (pH-8.0 with Na_2CO_3), stirred 30 min at 55°C. After that, centrifugation was done at 2000 g, 10 min, 4°C. The supernatant (1) was retained and cooled at 20°C, while pellets were again mixed with distilled water (pH 10 with Na_2CO_3) and stirred (30 min at 40°C). Again, centrifugation was done at 2000 g, 10 min, 4°C. The supernatant (2) was retained and cooled at 20°C. Supernatants (1) and (2) were mixed together, and the pH was adjusted to 4.5 with 20% HCl using a vigorous stirrer. Again, centrifugation was done at 2000 g, 10 min, 4°C, and the supernatant was retained and cooled at 10°C, and an equal volume of 100% chilled ethanol (EtOH) was added. Again, centrifugation was done at 2000 g, 10 min, 4°C. The pellet was retained, and air dried at RT for 3h and then hot dried at 60°C in a hot air oven.

2.5. Characterization of isolated barley β-glucan.

2.5.1. Anthrone test.

Carbohydrate content was quantified using the anthrone method [25] with glucose as the standard, with minor adjustments. Firstly, a glucose standard solution (1 mg/mL) was prepared and then diluted to create glucose concentrations ranging from 100-1000 µg/mL; the same was done for BBG, along with an unknown sample (BBG). A freshly prepared 0.2% anthrone reagent in sulfuric acid (3 mL) was added to each test tube. The tubes were placed in a water bath at 90°C for 10 minutes, during which the carbohydrates reacted with concentrated sulfuric acid to produce furfural. Absorbance was measured at 630 nm using a multimode microplate reader (Synergy H1, BioTek, USA).

2.5.2. Quantification of barley β-glucan by aniline blue staining.

Quantification of BBG through aniline blue staining was assessed in accordance with a previously reported protocol [26]. 1M NaOH was used to prepare the sample in various aliquots, from which 300µl of the sample was mixed with 6 M NaOH. Additionally, the BBG aliquots were heated (80°C, 30 min) in a water bath. Afterward, the sample was incubated at 50°C for 30 min, and 630 µL of aniline blue (21 portions 1 mol/L hydrochloric acid, 59 portions 1 mol/L glycine buffer at pH 9.0, 40 portions aniline blue solution 0.1% in water) was mixed and then incubated at RT for 30 min. The sample's fluorescence was measured at excitation and emission wavelengths of 400 and 500 nm, respectively.

2.5.3. Fourier transform infrared spectroscopy.

For the functional group examination of the BBG, FTIR analysis was used to confirm the nature of the compound. Using the OPUS software, 32 scans ranging from 4000 to 500 cm^{-1} were conducted for the BBG FT-IR analysis on the Bruker ALPHA II small FT-IR spectrometer [27].

2.5.4. UV-Visible spectroscopy.

UV-Vis spectroscopic examination for the presence of the distinctive absorption peak of BBG was performed using the previously reported [28] protocol, utilizing a UV-Vis spectrophotometer (UV-1900i, Shimadzu, Japan). The sample was prepared at 1 mg/mL in

distilled water, and a spectrophotometric scanning spectrum was obtained at a wavelength of 200–700 nm.

2.6. Antioxidant activity determination.

All antioxidant assays were conducted in triplicate (n=3) with Ascorbic Acid (AA) as the standard and distilled water as the blank. Data were represented as mean ± SD.

2.6.1. DPPH assay.

In the DPPH assay, evaluate the FRSA of the compound. The DPPH free radical scavenging activity was determined following the method [29]. 0.1mM DPPH was mixed in methanol to prepare DPPH. 2 mL of it was then mixed with various aliquots (20-100 µg/mL) of the extracted BBG. Aliquots were then incubated in the dark (30 min), and absorbance was taken at 517 nm using a multi-mode microplate reader (Synergy H1, BioTek, USA). % Radical scavenging activity was calculated using the following equation:

$$\text{RSA\%} = \frac{\text{Absorbance of control} - \text{Absorbance of sample}}{\text{Absorbance of control}} \times 100 \quad (1)$$

2.6.2. Reducing power assay (RPA).

To assess the reducing power (Fe^{+3}) to ferrous ion (Fe^{+2}) of BBG, RPA was performed according to the method [30] described with slight modification. Briefly, 2.5 mL of the various aliquots of the extracted BBG were obtained and prepared in distilled water (DW). 2.5 mL of phosphate buffer (PB) (0.2 M, pH=6.6), and 2.5 mL of 1% potassium ferrocyanide [$K_4Fe(CN)_6$] were added, then the reaction was thoroughly mixed and incubated (50°C, 20 min) on a water bath. Afterward, 2.5 mL of Trichloroacetic acid (TCA), 10% (w/v) was mixed in each tube and centrifuged (Thermo Scientific Sorvall ST8R, USA) at 3000 rpm, 5-6 minutes at 4°C. After centrifugation, the upper layer (2.5 mL) was taken, and 2.5 mL of DW was added and mixed properly. Further 0.5 mL (500 µl) of $FeCl_3$ (0.1 % w/v) was also added a bluish-colored solution was formed, and O.D. was taken at 670 nm wavelength on a multimode microplate reader (Synergy H1, BioTek, USA).

2.6.3. Hydrogen peroxide (H_2O_2) scavenging activity.

H_2O_2 scavenging activity potential was investigated according to the previously described method [30]. BBG was taken in different concentrations and suspended in phosphate buffer. A 43 mM H_2O_2 solution was prepared in phosphate buffer (0.1 M, pH 7.4). Prepared concentrations of BBG were then taken in the amber-colored Falcon tube. Then, 3.4 mL of phosphate buffer (0.1 M) was mixed into each tube, and 0.6 mL (600 µL) of 43 mM H_2O_2 solution was added and incubated for 15 min at RT. The absorbance was taken on a UV-visible spectrophotometer (UV 1900i, Shimadzu, Japan) at 230 nm. H_2O_2 solution (without extract) was taken as a control. The % H_2O_2 scavenging activity was calculated using the following equation.

$$\%\ \text{Scavenged}\ [H_2O_2] = \frac{\text{Absorbance of control} - \text{Absorbance of sample}}{\text{Absorbance of control}} \times 100 \quad (2)$$

2.6.4. ABTS assay.

The antioxidant activity of BBG was also assessed using the 2,2'-azino-bis(3-ethylbenzothiazoline-6-sulfonic acid) (ABTS) radical scavenging assay as previously described [30]. In brief, the ABTS+ radical solution was prepared by adding 2.4 mM potassium persulphate and 7 mM ABTS solution in an equal ratio and keeping them in the dark at RT (25°C) for 24 h. Later, the prepared ABTS+ reagent was diluted with DW to obtain an absorbance of 0.7±0.01 units at 650 nm. BBG at different dilutions was reacted with ABTS+ solution (80 µL) in a 96-well plate & incubated at RT for 4 min. The O.D. at 650 nm was read using a multi-mode microplate reader (Synergy H1, BioTek, USA). ABTS+ solution was used as a control. ABTS radical scavenging assay was calculated using the following formula.

$$\text{Scavenged ABTS Radical \%} = \frac{\text{Absorbance of control} - \text{Absorbance of sample}}{\text{Absorbance of control}} \times 100 \quad (3)$$

2.6.5. Ferric reducing antioxidant power (FRAP assay).

The FRAP assay was performed according to the previously described method [31] with minor modifications to assess the potential of BBG to reduce ferric ions. Different concentrations (20-100 µg/mL) of BBG were taken (100 µL added) with the 3 mL FRAP reagent, i.e., composed of 300 mM CH_3COONa (sodium acetate) buffer (pH=3.6), 10 mM TPTZ (2,4,6- Tri(2-pyridyl)-s-triazine solution), and 20 mM $FeCl_3$ in the ratio of 10:1:1, respectively. The reaction was incubated (37°C for 30 min), and O.D. was read at 593 nm on a multi-mode microplate reader (Synergy H1, BioTek, USA).

2.7. Hemolysis assay.

To determine the hemolytic effect of the BBG against RBCs, the hemolysis assay was performed as per the previous protocol with slight modifications [29]. Briefly, 5 mL of the blood was washed 3X with saline, centrifuged, and diluted with saline. 200µl of the diluted blood (in an equal ratio of saline) was mixed with different aliquots (20-100 µg/mL) of BBG and incubated for 3 h at 37°C. Triton-100X was utilized as a +ve control for the 100% lysis of RBCs, and saline was used as a -ve control. O.D. was recorded at 570 nm by a multimode microplate reader (Synergy H1, BioTek, USA). The given formula calculated the % hemolysis:

$$\text{\% Hemolysis} = \frac{\text{Absorbance of sample} - \text{Absorbance of negative control}}{\text{Absorbance of Positive control} - \text{Absorbance of negative control}} \times 100 \quad (4)$$

2.8. Anticancer activity determination.

2.8.1. Cell viability assay.

Cell viability of BBG was assessed using the MTT assay, following the previously described protocol [29]. Briefly, A549 cells (1x 10^4 cells/well) were seeded in a 96-well plate and incubated at 37°C for 24 h. Cells were then treated with various concentrations of BBG for 24 h. After treatment, 10 µL MTT dye was added, and the cells were further incubated for 4 h at 37°C. Absorbance was read by a multi-mode microplate reader (Synergy H1, BioTek, USA) at 545 nm, and cell viability% was calculated with the given formula. All experiments were performed in triplicate (n=3), and results were expressed as mean ± S.D.

$$\text{Cell Viability\%} = \left(\frac{\text{Absorbance of treatment}}{\text{Absorbance of control}}\right) \times 100 \quad (5)$$

2.8.2. Determination of nuclear morphology using Hoechst staining.

Hoechst staining was performed according to a previously reported protocol [32]. A 12-well plate was seeded with 5×10^4 cells/well and incubated. Cells were exposed to various aliquots of BBG, and the plate was incubated at 37°C for 24 hrs. Cells were then washed with PBS after 24 h, and an additional 10 µL of Hoechst was added for 15 minutes. Images were captured using an EVOS FLoid Imaging microscope.

2.8.3. PI/ Propidium iodide staining for the detection of apoptosis.

PI staining was performed according to the protocol with minor modifications [29]. Briefly, 5×10^4 cells/well were seeded in a 12-well plate & incubated overnight. Further, cells were exposed to various aliquots of BBG and then incubated for 24 h. Afterward, cells were stained with 1µg/mL of PI, and then incubation was done (10 min at 37°C). The images were attained by using the EVOS FLoid imaging microscope.

2.8.4. Hoechst and PI dual staining.

To examine apoptosis and nuclear morphology concurrently, Hoechst and PI dual staining was performed, according to [32]. Hoechst and PI staining were combined with the filters used for the imaging. A549 cells were cultured in DMEM for 24 h, then treated with BBG and incubated for 24 h. Afterward, the cells get washed with PBS, and then cultured with 10µL Hoechst and 10 µL PI dye and incubated for 15 min. Finally, the cells were again washed with PBS and examined under an EVOS FLoid imaging microscope.

2.8.5. Reactive oxygen species (ROS) generation.

Reactive oxygen species (ROS) generation was measured according to the previously described protocol [33]; 5×10^4 cells/well were seeded in a 12-well plate and incubated overnight at 37°C. After 24 h of incubation, cells were cultured with various aliquot doses of BBG and further incubated for 24 h. After incubation, H2DCFDA (10 µM, 15 min) was used to screen cellular ROS generation, and a microscopy image of ROS was obtained.

2.8.6. Acridine orange and Ethidium bromide (AO/EtBr) staining.

AO/EtBr dual staining was performed according to the previously described protocol with minor modifications [29]. 5×10^4 cells/well seeded in a 12-well plate and incubated for 24, further treatment with various concentrations of BBG was given, and incubation was done for 24 h. Further, cells were stained with 5 µL of AO and 5 µL EtBr (5 mg/mL each), and cells were observed with an Evos FLoid Imaging microscope.

2.9. Statistical analysis.

All experiments were conducted in triplicate (n=3) and expressed as mean ± SD or SEM Initially, a Microsoft Excel worksheet was used for data collection and summarisation. An analysis of variance (ANOVA) with a significant p-value <0.05, **p-value <0.01, *** p-value <0.001, and *** p-value <0.0001 was conducted on GraphPad Prism 8.0 software (GraphPad Software, Inc., La Jolla, USA). ImageJ software was used to calculate fluorescence intensity for experiments involving cell-based assays.

3. Results and Discussion

3.1. ADMET properties of β-glucan.

BBG was shown as an extremely polar molecule due to its seven rotatable bonds and sixteen hydrogen bond acceptors. With 11 hydrogen bond donors, it showed a high potential for biological system interactions. With a molar refractivity of 100.5, it appeared to have a big volume and would have trouble passing through biological barriers. The molecule was stiff and fully saturated with a proportion of sp3 hybridized carbons of 1.5. Its high Topological Polar Surface Area (TPSA) of 268.68 Å² indicates considerable polarity, which may contribute to its inability to cross lipophilic barriers, such as the blood-brain barrier (BBB). Improved gut health or improved cholesterol management are two benefits that BBG may offer, as it is stored in the digestive tract [34]. Shelf life and product structure may benefit from the molecule's stability under a range of conditions due to its rigidity and full saturation. The detailed pharmacokinetic profile of BBG is given in Table 1.

Table 1. Pharmacokinetic properties of β-glucan.

Properties	Factors	β-glucan (expected values)
Physicochemical properties	MW (g/mol)	504.44g/mol
	Number. rotatable bonds	7
	Num. H-bond acceptors	16
	Number. H-bond donors	11
	Molar Refractivity	100.5
	Fraction Csp3	1
	TPSA	268.68 Å²
Lipophilicity Log p o/w	iLOGP	-0.26
	XLOGP3	-6.88
	WLOGP	-7.57
	MLOGP	-6.15
	SILICOS-IT	-6.49
	Consensus Log P o/w	-5.47
Absorption	Water solubility Log S (ESOL)	1.83
	GI absorption	low
	Skin permeation (Log Kp) (cm/s)	-14.26
	P-gp substrate	Yes
Distribution	BBB permeant (log BB)	-1.367
	CNS permeation (log PS)	-5.425
	VDss (log L/Kg)	-0.449
	Fraction unbound (Fu)	0.487
Metabolism	CYP2D6 substrate	No
	CYP3A4 substrate	No
	CYP1A2 inhibitor	No
	CYP2C19 inhibitor	No
	CYP2C9 inhibitor	No
	CYP2D6 inhibitor	No
	CYP3A4 inhibitor	No
Excretion	Total clearance (log mL/min/kg)	1.623
	Renal OCT2 substrate	No
Toxicity profile	Ames toxicity	No
	Max. tolerated dose (human) (log mg/kg/day)	0.543
	hERG I inhibitor	No
	hERG II inhibitor	Yes
	Oral rat acute toxicity (LD50)	2.879
	Oral rat chronic toxicity (LOAEL) (log mg/kg/bw/day)	5.241
	Hepatotoxicity	No
Drug likeness	Lipinski violations	Yes
	VEBER violations	Yes
	Bioavailability score	0.17
Medicinal chemistry	PAINS alerts	0 alert
	Synthetic accessibility	6.45

Properties	Factors	β-glucan (expected values)
	Leadlikeness	No;1 violation: MW>350

TPSA: Topological Polar Surface Area; Log P o/w: Partition Coefficient between octanol and water; iLOGP: Predicted Log P (iLOGP method); XLOGP3: Predicted Log P (XLOGP3 algorithm); WLOGP: Predicted Log P (Wildman–Crippen); MLOGP: Predicted Log P (Moriguchi method); Consensus Log P: Average Log P from models; Water solubility Log S: Predicted water solubility; GI absorption: Gastrointestinal Absorption; Skin permeation (Log Kp): Skin permeability coefficient; P-gp substrate: P-glycoprotein substrate; BBB permeant (log BB): Blood–Brain Barrier permeability; CNS permeation (log PS): Central Nervous System permeability; VDss: Steady-State Volume of Distribution; Fu: Fraction unbound in plasma; Total clearance: Drug elimination rate; Ames toxicity: Mutagenicity test; Max. tolerated dose: Maximum safe dose in humans; hERG I inhibitor: Cardiac potassium channel inhibitor; hERG II inhibitor: Cardiac ion channel inhibitor; LD_{50}: Median lethal dose; LOAEL: Lowest Observed Adverse Effect Level.

3.2. ProTox-3.0-prediction of toxicity of chemicals.

Toxicity prediction of BBG showed that it comes under class 3 in predicted toxicity, with LD_{50} at 51 mg/kg (toxic if swallowed ($50 < LD_{50} \leq 300$ with 100% prediction accuracy).

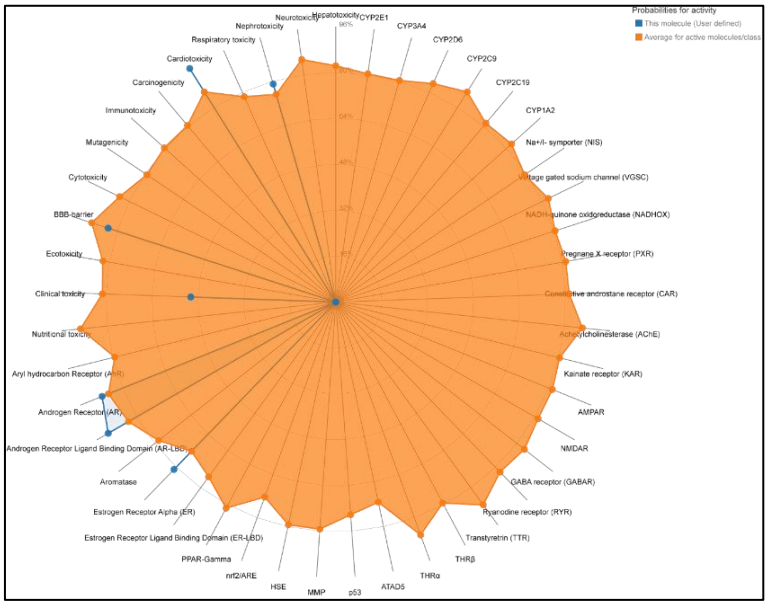

Figure 1. Toxicity radar chart. The blue dots show the molecule (user-defined), and the orange dots represent averages of active molecules/class.

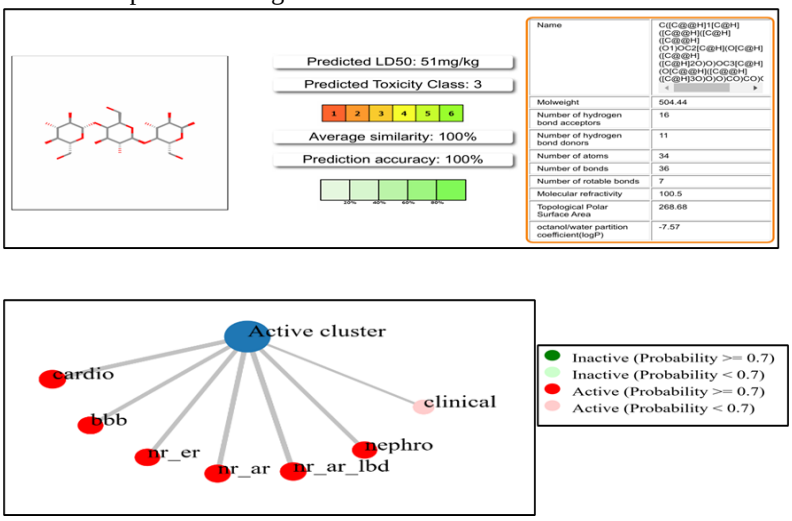

Figure 2. Predicted report and network chart showing the active clusters with active probability >=0.7 and <0.7.

It showed toxicity in a few targets (nephro, cardio, bbb, clinical, nr_ar, nr_ar_lbd, ne_er) as shown in Figure 1 and Figure 2. The toxicological profile of BBG showed it to be non-toxic and raised long-term safety concerns.

3.3. Network pharmacology

3.3.1. Swiss target prediction.

The analysis of BBG revealed a wide variety of possible molecular targets. It is anticipated that a sizable percentage, 33.3%, may interact with protein-coupled receptors of the Family A G. Enzymes (13.3%), various cytosolic proteins (26.7%), and secreted proteins (20%) are other noteworthy targets. Kinases were predicted to be the target of a lower percentage, 6.7%, as shown in Figure 3.

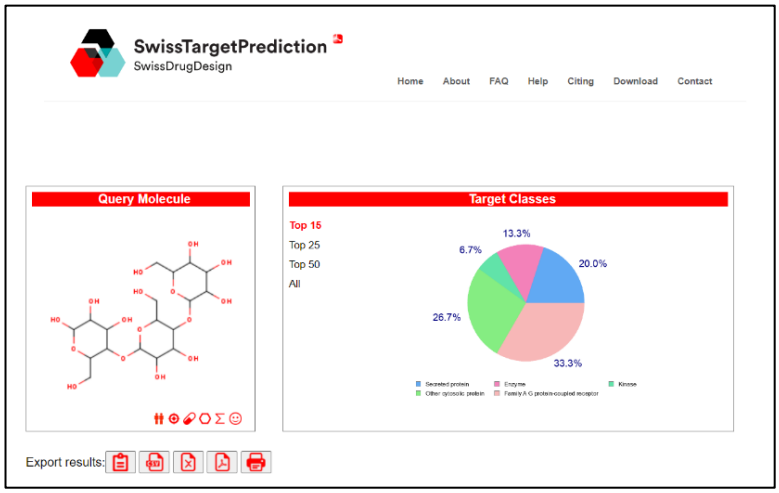

Figure 3. Target prediction analysis of β-glucan showing the target classes.

3.3.2. Common target finding by Venny 2.1.0.

GeneCard was used to select the top ~25K targets related to LC, which were then merged with the BBG (100) targets obtained by target prediction. Using Venny 2.1.0, the common targets in both were found (95), which were then documented as applicant targets as shown in Figure 4.

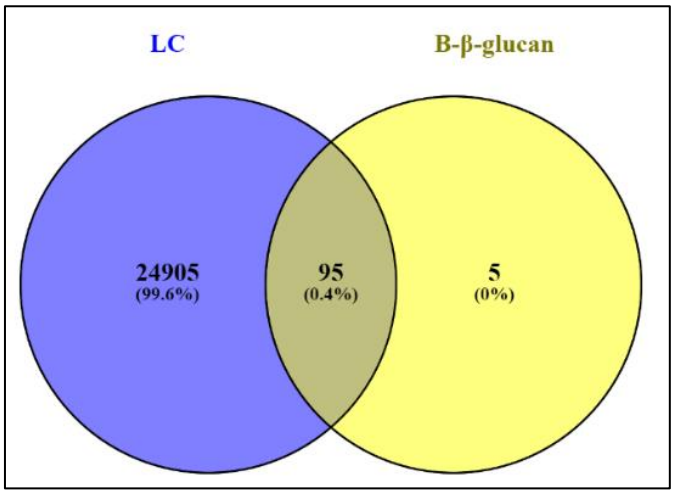

Figure 4. Venn diagram preparation for common target finding by Venny 2.1.0.

Common targets were further used to make the PPI network by the STRING tool, which was then further rectified by Cytoscape software, as shown in Figure 5. Our *in-silico* analysis of BBG showed that it could target or bind with 95 LC-related targets, out of which 19 targets showed a high degree of closeness and could influence the cancer cells.

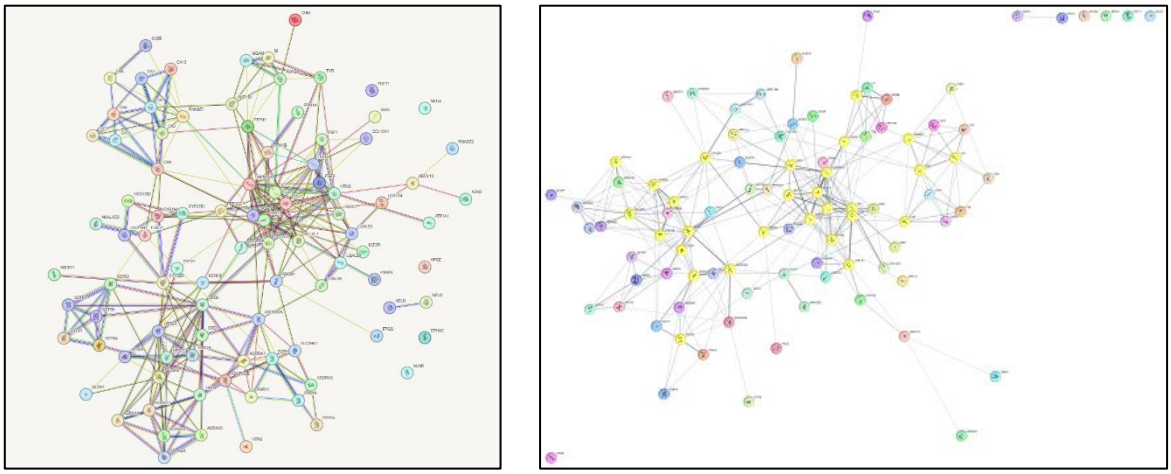

(a) **(b)**

Figure 5. Protein-ligand interaction, **(a)** PPI network formation by the STRING tool; **(b)** Utmost degree-wise selection of targets through Cytoscape 3.10.2 software.

3.4. Molecular docking.

Protein-ligand docking endeavors to forecast the ligand's (BBG) capacity to suppress the activity of LC-related proteins from the perspective of binding position and binding affinity. A relationship between two molecules can be identified by measuring the strength of the interaction, which is known as binding affinity [35]. The strength and stability of the molecular connection increase with decreasing binding affinity value [36]. Ligands bind to the active site (A-site) of the protein with the least binding affinity, and under the ATP-binding affinity are forecast to constrain protein activities. The top 18 candidates were nominated for MD based on the network pharmacology and PPI network. The precise docking affinity and bonds of BBG with targets are shown in Table 2. Docking results show that ligands bind to the A-site of the targeted protein with the least binding affinity (CDK1 (4YC6) -8.2 kcal/mol, ABCB1(7OTI) -7.6 kcal/mol, and ADORA2A (6GDG) -7.5 kcal/mol). Consequently, with binding to the proteins' A-site and having lower binding energy than BBG, it is predicted to be able to inhibit the targeted proteins of LC. 2D and 3D structures of given interactions of ligands and selected proteins are shown in Figure 6. In mammals, CDK1 is crucial to cell cycle progression (as it promotes G2/M and G1/S transitions, in addition to G1 progression too) [37]. CDKs are highly expressed in NSCLC with EGFR mutations. CDK1 could be a potential target for cancer prevention and therapy [38,39]. The ABCB1 (ATP-binding cassette sub-family B) target interacts with BBG through conventional hydrogen bond interactions with amino acids, including ARG144, VAL175, SER176, ASN179, LEU920, TYR924, and LYS930. ABCB1 genes, also known as MDR1 (multidrug resistance), encode for p-glycoprotein (P-gp), a membrane-associated ATP-reliant transporter, which acts as an efflux pump expressed on the surface of cancer cells. P-gp is often up-regulated among numerous cancer forms (lung, ovarian, and breast cancer). BBG may reduce the expression of the ABCB1 gene [40]. The interaction between ADORA2A (adenosine A2a receptor) with BBG through SER35, TYR37, GLN38, ASP240, and SER334, with a conventional hydrogen bond. The adenosine A2a receptor (ADORA2A) is a member of the G protein-coupled receptor (GPCR) superfamily.

Table 2. Protein-ligand interaction of the top 3 targets with PDB ID, Affinity Kcal/mol, Interactions, Site Attributes, interacting amino acids, and RMSD Å.

Targets	PDB ID	Affinity Kcal/mol	Interactions	Site attributes	Interacting amino acid residues	RMSD (Å)
CDK1	4YC6	-8.2	Carbon hydrogen, conventional hydrogen, unfavorable donor-donor bond	X= -4.220 Y= 34.627 Z= -16.064	GLN49; LYS89; ARG44; VAL48; ASP86; LEU83; ASP146; GLN132	2
ABCB1	7OTI	-7.6	Conventional hydrogen, unfavorable donor-donor bond	X= 114.605 Y= 113.170 Z= 119.358	LYS930; LEU920; TYR924; ARG144; VAL175; ASN179; SER176	1.68
ADOR A2A	6GDG	-7.5	conventional hydrogen bond	X= 78.344 Y= 89.476 Z= 76.209	GLN38; SER334; ASP240; TYR240; TRY37 ARG42; SER35	2.48
FN1	3M7P	-7.3	Conventional hydrogen, unfavorable donor-donor bond	X= 29.424 Y= 43.839 Z= -20.325	GLU377; GLY378; ARG592; GLU596; THR376; THR375; GLU537	1.86
BCL2L 1	6O0K	-7.2	Carbon-hydrogen, conventional hydrogen bond	X= -11.894 Y= 2.026 Z= -17.418	HIS184; ARG127; TYR180; ALA131; VAL134; GLU135	25.78
CYP2D 6	5TFT	-7	Conventional hydrogen, an unfavorable acceptor-acceptor bond	X= -19.709 Y= 26.183 Z= -66.507	THR76; ASN225	1.95
CA9	2HFK	-7	Van der Waals, carbon-hydrogen bond, conventional hydrogen bond	X= -4.514 Y= 10.396 Z= -1.450	TYR101; GLY102; THR97; VAL99; ARG50; SER96; PHE101; TYR37; ASN33; ARG52; ALA33; SER53; TYR32; SER55; ASN56; ASN31	2.07
CASP3	2CJY	-6.9	Conventional hydrogen, unfavorable acceptor-acceptor, unfavorable donor-donor bond	X= 36.905 Y= 32.442 Z= 30.047	SER209; ASN208; TRP214; SER251; ARG207	1.98
PTPN1	2QBP	-6.8	Conventional hydrogen, unfavorable acceptor-acceptor, unfavorable donor-donor bond	X = 47.007 Y = 14.980 Z = 6.614	HIS60; THR138; THR164; ASN139; ASN162; THR165; GLU167; LYS103; TRP100 ARG169	1.65
DRD2	6CM4	-6.7	carbon hydrogen, conventional hydrogen, unfavorable acceptor-acceptor, Pi-donor hydrogen bond	x= 19849 Y= -2799 Z= 23.86	ASP1070; ALA1074; PHE1104; GLY1030; VAL1103	1.88
HSP90 AA1	5NJX	-6.7	Conventional hydrogen bond	X= -33.430 Y= 24.272 Z= -13.169	TRP297; LYS254; GLU255	2
IL2	6VW U	-6.5	Carbon hydrogen, conventional hydrogen, unfavorable donor-donor bond	X = -79.649 Y = 83.43 Z = 55.978	ARG255; ILE148; GLU254; PHE153; THR152	3.81
STAT3	6NJS	-6.4	Carbon-hydrogen, conventional hydrogen bond	X= -1.166 Y= 10.216 Z= 25.992	CYS251; SER514; ASP334; ALA250	1.3
HTR2A	6WG T	-6.3	Conventional hydrogen bond	X = 23.937 Y = 36.982 Z = 50.819	ASN363; LYS223; ASP356	2.01
RNASE 1	2PQX	-6.3	Carbon-hydrogen, conventional hydrogen bond	X = 33.089 Y= 5.657 Z = 34.284	ASP50; GLU114; LEU41; SER113; GLU38	2.09
LGALS 3	1KJL	-5.6	Carbon-hydrogen, conventional hydrogen, unfavorable donor-donor bond	X = -76.649 Y = 83.430 Z = 55.978	GLN150; ASP148; GLY235; SER237; ARG144	2.68
FGF2	4L0R	-5.6	Van der Waals, conventional hydrogen bond	X= 16.023 Y= 3.738 Z= 11.987	GLU36; SER39; GLN43; GLN51; GLN46; LEU42; ARG97; GLN100; GLU104; ASN35;	2.09
HRAS	8CXF	0.02	Carbon-hydrogen, conventional hydrogen, unfavorable acceptor-acceptor bond	X = 59.84 Y = 12.787 Z = 15.078	DG:2; DC:3; DG:26; DT:12	59

BBG may suppress the expression of ADORA2A, which may influence the immune system against cancer cells [41].

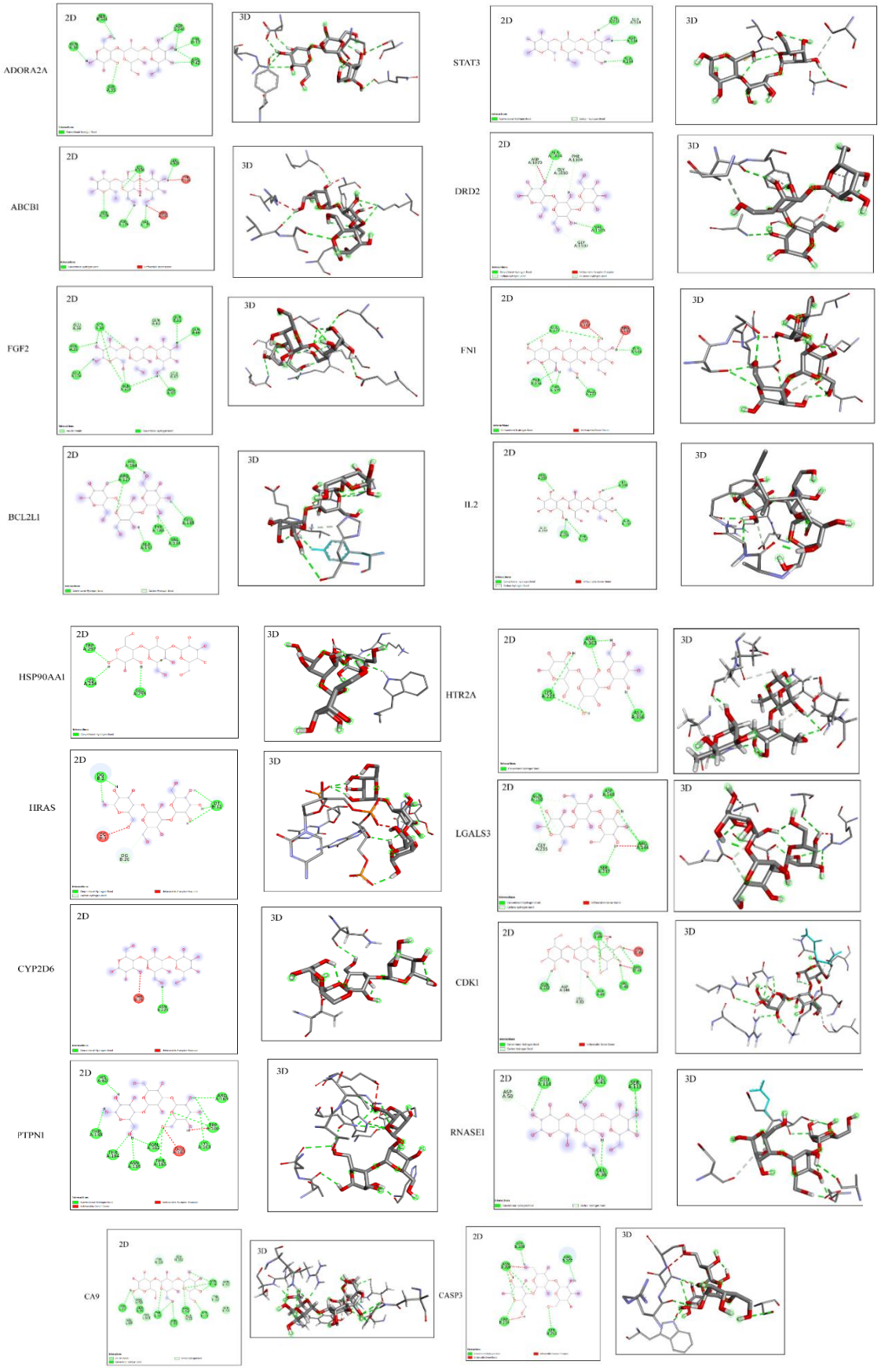

Figure 6. 2D and 3D structures of ligand and candidate proteins binding interactions.

3.5. Extraction of BBG.

BBG was extracted using an alkaline/acidic extraction procedure, followed by hot-air drying. After drying in a hot-air oven, 20 g of barley powder yielded 1.322 g of gummy β-glucan in a light tan-colored gum form, as shown in Figure 7. The total yield was 6.61%.

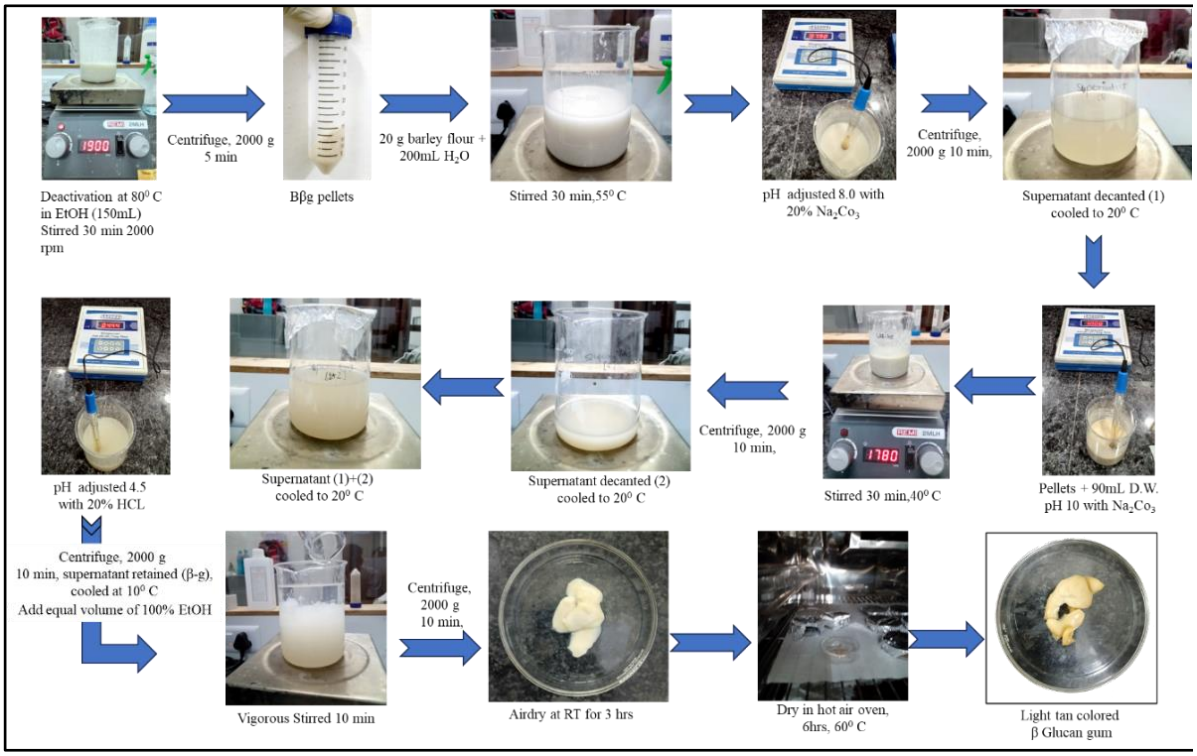

(a)

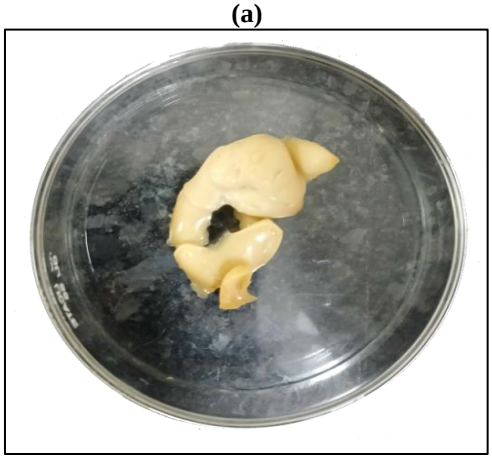

(b)

Figure 7. (a) β-glucan extracted from barley protocol; **(b)** Hot dried β-glucan (appeared as tan-colored gum).

3.6. Characterization of extracted BBG.

3.6.1. Anthrone test for quantitative estimation of carbohydrate.

Sulfuric acid and anthrone reagent were mixed to create an anthrone reagent solution. A blue-green color compound was produced when this solution was mixed with the sugar aliquots (100–1,000 µg/mL) and the BBG sample (unknown concentration), as depicted in Figure 8. The quantitative estimate test revealed that the concentration of the unknown was 550 µg/mL.

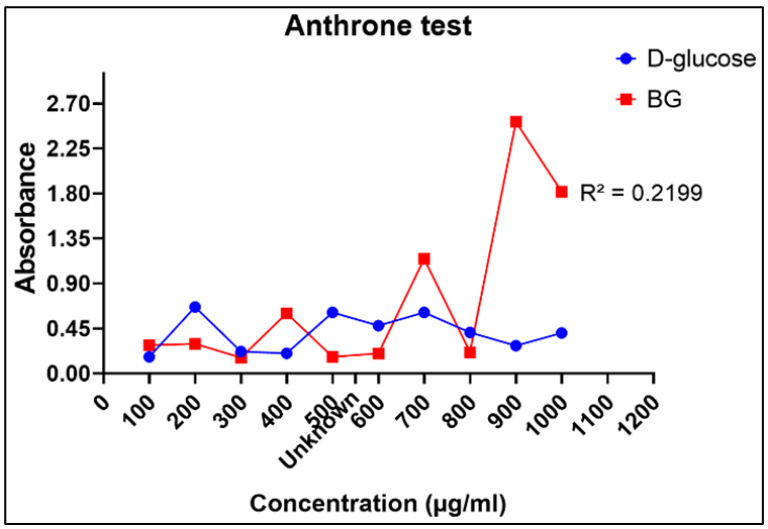

Figure 8. An anthrone test to quantify the carbohydrate content in BBG revealed that the concentration of the unknown was 550 µg/mL. The R^2 value was 0.2199.

3.6.2. Quantification by aniline blue staining dye to confirm the presence of β-1, 3 linkages in extracted β-glucan.

Aniline blue precisely reacts to the single-helical conformation of the β-1, 3-glucan, subsequently showing fluorescence emission. Our results showed that fluorescence intensity increased as depicted in Figure 9, with the increase in concentration of the BBG, thus ensuring the occurrence of the β-1,3 linkages in the isolated BG from barley.

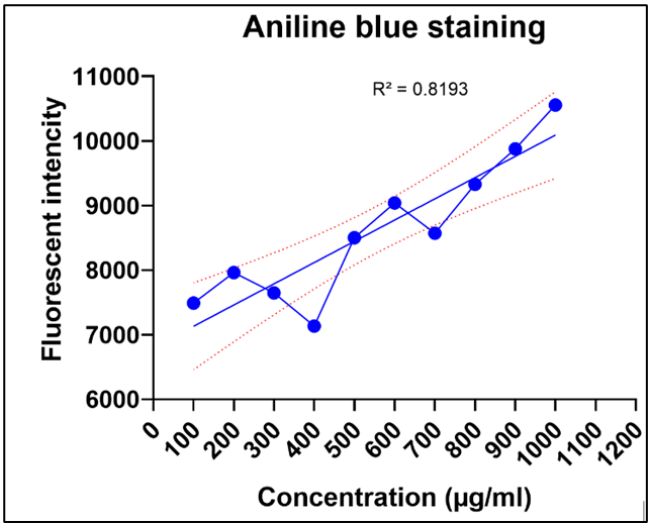

Figure 9. Aniline blue staining for quantitative analysis of BBG, fluorescence intensity elevated with dose, validating the detection of β-1,3 linkages in isolated BBG, $R^2 = 0.8193$.

3.6.3. Fourier transform infra-red spectroscopy.

FTIR spectra were recorded and compared with the BBG spectra observed by [42]. FTIR examination spectra were noted between 4000 and 500 cm^{-1}, and % transmittance was seen. In spectra, the BBG band at a wavenumber of 890 was for β-linked polymer, 1,076 = C–O stretch, 1,372 = CHOH stretch, 2,919 = C–H stretch, and 3,390 = OH stretch. An analogous spectrum by a minor variance was seen in our investigation of BBG transmission spectra, Figure 10. The peak at 894 showed β-linked polymer, and 1,023 favored the presence of C–O stretch. The peak at 1,373 specified the CHOH, and 2,926 designated the C–H stretch. At 3,328

OH stretch was found. All these points were revealing of the β1,3 as the chief linkage existing in the BBG. The obtained spectra were in the range of various previously reported studies [43,44].

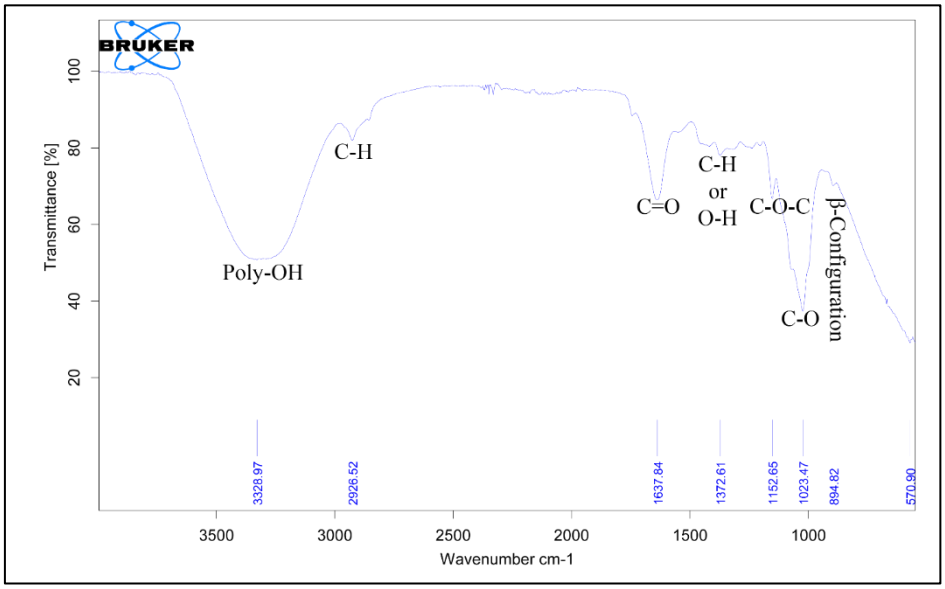

Figure 10. FTIR spectrum of BBG, verifying β-1,3 linkages with distinctive peaks at 894, 1023, 1373, 2926, and 3328 cm^{-1}.

3.6.4. UV-visible spectrum scanning for monosaccharide composition of β-glucan.

D-glucose was the dominant monosaccharide in BBG [27]. Figure 11 shows a valid curve as per the reported studies [29], conforming to the presence of monomer (D-glucose) in BG.

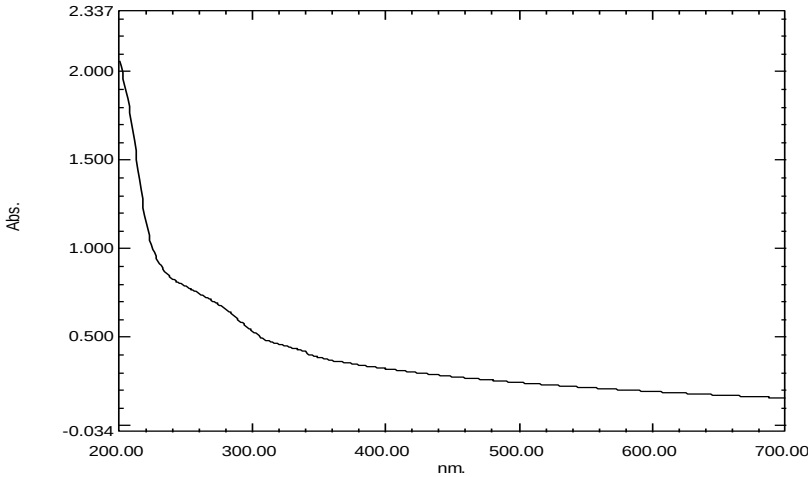

Figure 11. UV-Vis spectrum of BBG (200–700 nm), revealing a trend corresponding to D-glucose monosaccharide.

3.7. Antioxidant activity determination.

3.7.1. DPPH assay

Antioxidant activity was measured using DPPH. Previously reported a steady trend in scavenging activity as concentration increased [30]. An analogous trend with a minor variance was seen in our investigation of BBG (IC50 was measured at 45.06 µg/mL as shown in Figure 12, and showed a significant antioxidant capacity (* p value < 0.01). The data are presented as the average of 3 trials.

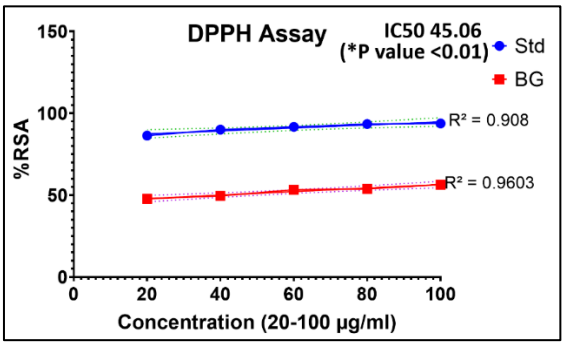

Figure 12. DPPH assay for antioxidant capacity determination, IC_{50} was 45.06 µg/mL and disclosed a noteworthy * p value < 0.01 antioxidant potency.

3.7.2. RPA assay.

Reducing power is a colorimetric technique that transfers electrons from an antioxidant to an oxidant. It assesses the antioxidant's capacity to reduce the blueish ferric tripyridyltriazine complex to its Fe^{2+} state [45], causing the absorbance to vary as illustrated in Figure 13. A substantial (*p-value <0.01) antioxidant capacity was found in our investigation, and it was revealed that absorbance rose as concentration increased.

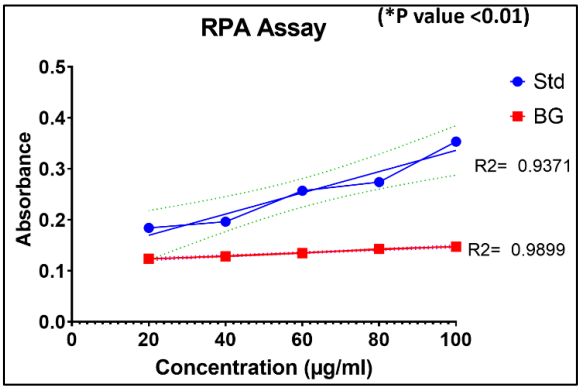

Figure 13. RPA assay for antioxidant capacity determination of BBG, in proportion to the dose (*p-value <0.01).

3.7.3. H_2O_2 assay.

The capability of BBG on hydrogen peroxide (H_2O_2) is shown in Figure 14. The BBG was capable of scavenging H_2O_2-free radicals in a dose-specific manner (20-100 µg/mL) and showed significant RSA (*P-value<0.05).

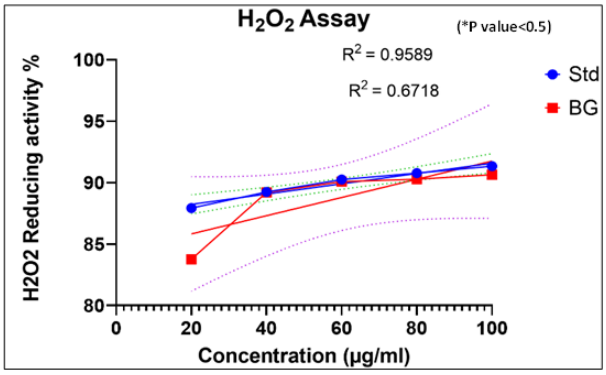

Figure 14. Scavenging competence of BBG on H_2O_2. BBG exhibited dose-specific % H_2O_2 reducing activity (20-100 µg/mL), with noteworthy RSA detected (*P-value < 0.05).

3.7.4. ABTS assay.

The RSA of BBG was assessed using the 2,2'-azino-bis (3-ethylbenzothiazoline-6-sulfonic acid). The percentage of RSA increased as the concentration of BBG (ns) and the standard deviation increased. (IC_{50} was measured at 49.86 µg/mL) as shown in Figure 15.

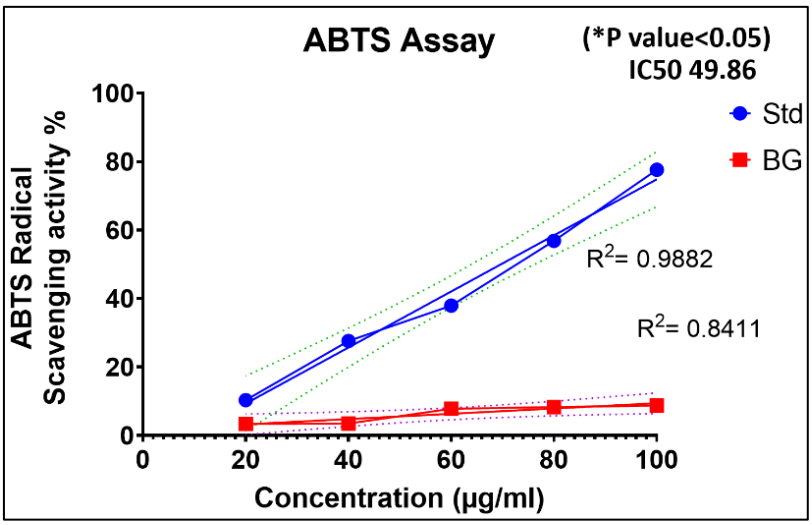

Figure 15. RSA of BBG was assessed using the ABTS assay. RSA was elevated with BBG and AA concentration, with an IC_{50} of 49.86 µg/mL.

3.7.5. FRAP assay.

The FRAP experiment was evaluated to assess the antioxidant capacity of BBG, showing that BBG has a significant antioxidant capacity (*** p<0.0001), increasing dose-dependent ferric-reducing (Fe^{+3} to Fe^{+2}) antioxidant activity as demonstrated in Figure 16.

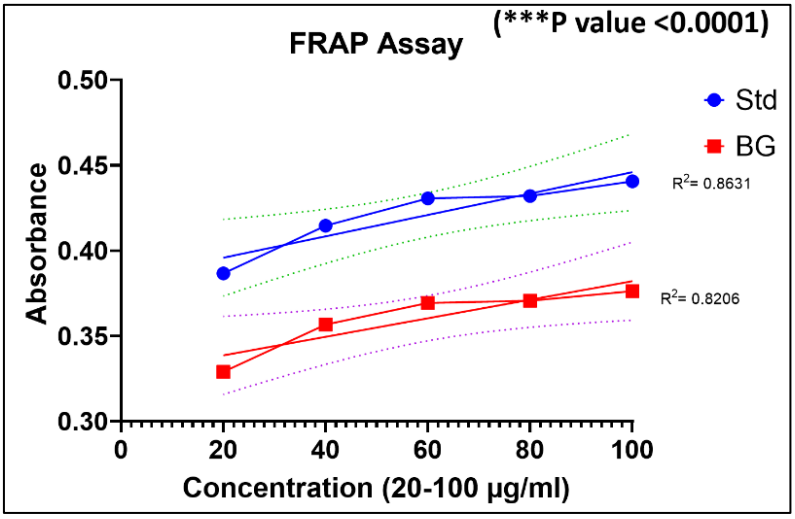

Figure 16. FRAP assay assessing the antioxidant capacity of BBG. BBG exhibited noteworthy (p< 0.0001) and Fe^{3+} to Fe^{2+} reducing antioxidant activity in proportion to dose.

3.8. Determination of hemolysis.

The biosafety of the BBG was assessed *in vitro* by evaluating its biocompatibility. Figure 17a shows that hemolytic inhibition activity increased with increasing concentration at higher doses when RBCs were exposed to BBG at 20-100 µg/mL for these fresh RBCs. As shown in Figure 17b, BBG does not cause RBC lysis. Hemolysis activity was low for BBG in our study, indicating its biocompatibility and low toxicity.

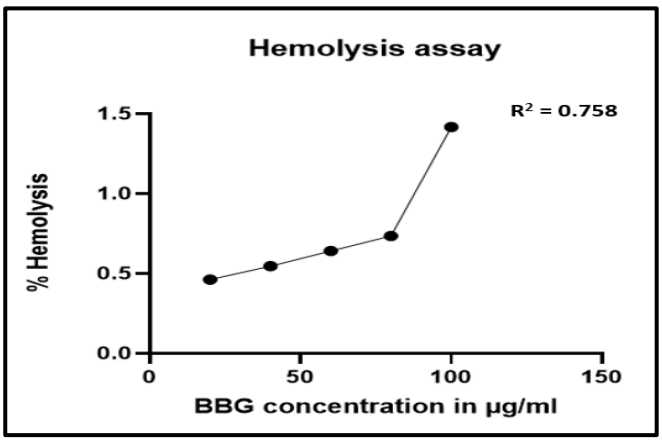

(a)

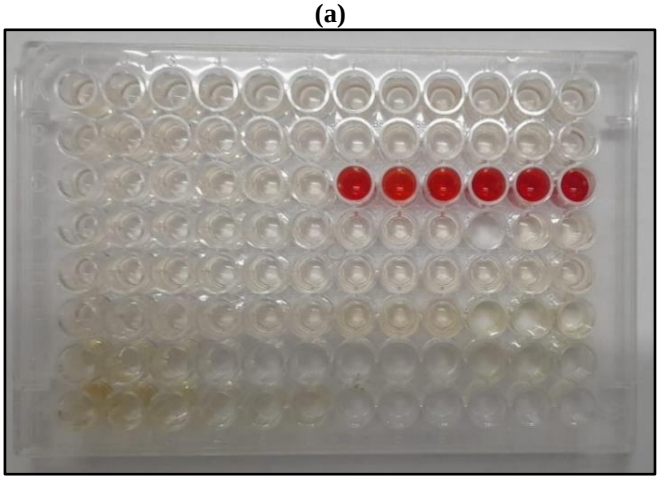

(b)

Figure 17. (a) Hemolysis assay. No significant hemolysis of RBCs was observed in comparison to the positive control (Triton X100); **(b)** 96-well plate of Hemolysis assay.

3.9. Determination of anticancer activity

3.9.1. Cell viability assessment by MTT assay.

The cytotoxicity potential of BBG and Cis against A549 cells was assessed using a cell viability assay [46]. Results indicated the decay in the metabolically active live (A549) cells. Figure 18 (a-b). The IC_{50} value was measured at 90 µg/mL, and the Cis IC_{50} value was 24 µg/mL. A similar study [47] showed that the cell viability assay of BBG on A549 cells has a similar effect as in our study.

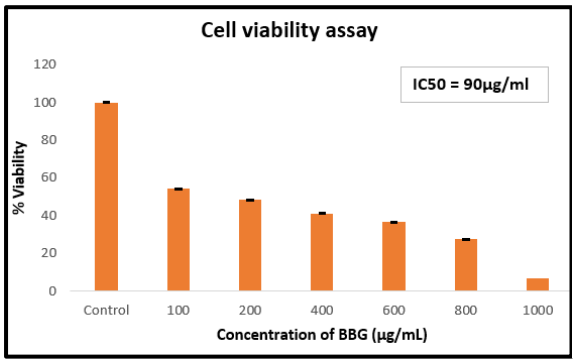

(a)

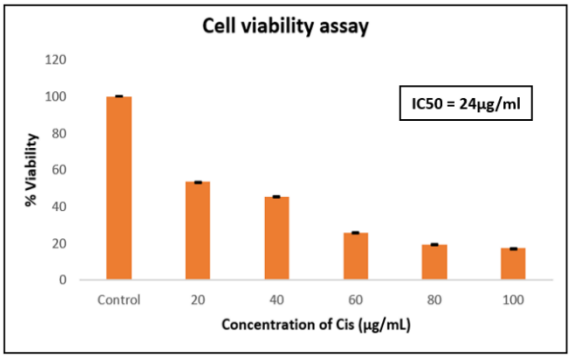

(b)

Figure 18. (**a**) Cytotoxic effect of BBG on A549 cell line viability, with an IC_{50} of 90 µg/mL. (**b**) Effect of cisplatin on A549, with an IC_{50} of 24 µg/mL.

3.9.2. Cell viability assessment, The effect of BBG on normal fibroblast cells (L929 cell line).

The cytotoxicity of BBG was assessed on the L929 cell line. Our findings showed that when exposed to increasing BBG concentrations, L929 cells had noticeably greater vitality than A549 cells, Figure 19. The IC_{50} value was measured at a higher concentration of 2.5 mg/mL.

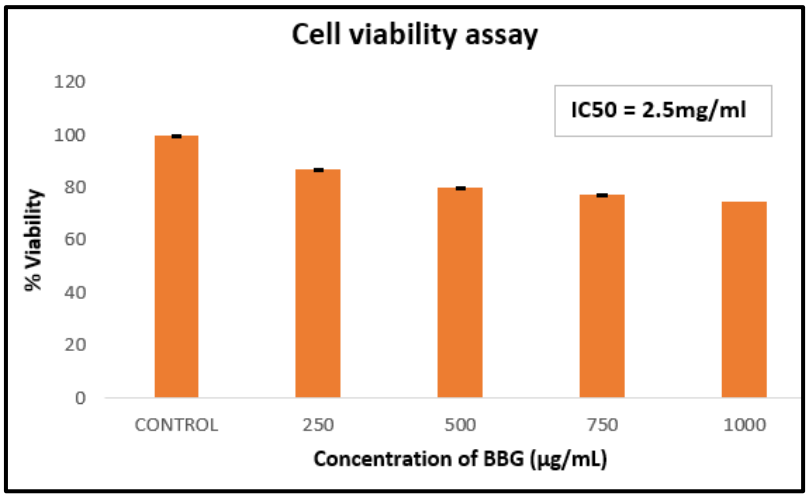

Figure 19. Cytotoxic effect of BBG on normal fibroblast cell lines (L929 cells), with an IC_{50} of 2.5 mg/mL.

3.9.3. Nuclear morphology examination by Hoechst staining.

Hoechst dye is unique in its ability to interact with the cell nucleus. It is a dye that binds to DNA and, when it does so, produces a blue fluorescence. This dye makes it simple to see any DNA abnormalities [48]. Our results show that while the nuclei in the treatment wells have lost part of their nuclear morphology, those in the control wells maintain a consistent shape. Figure 20 shows dose-dependent nuclear deformations, demonstrating the effective anticancer action of BBG. The greatest nuclear alterations occurred at 150 µg/mL. The yellow color arrow indicates nuclear deformations.

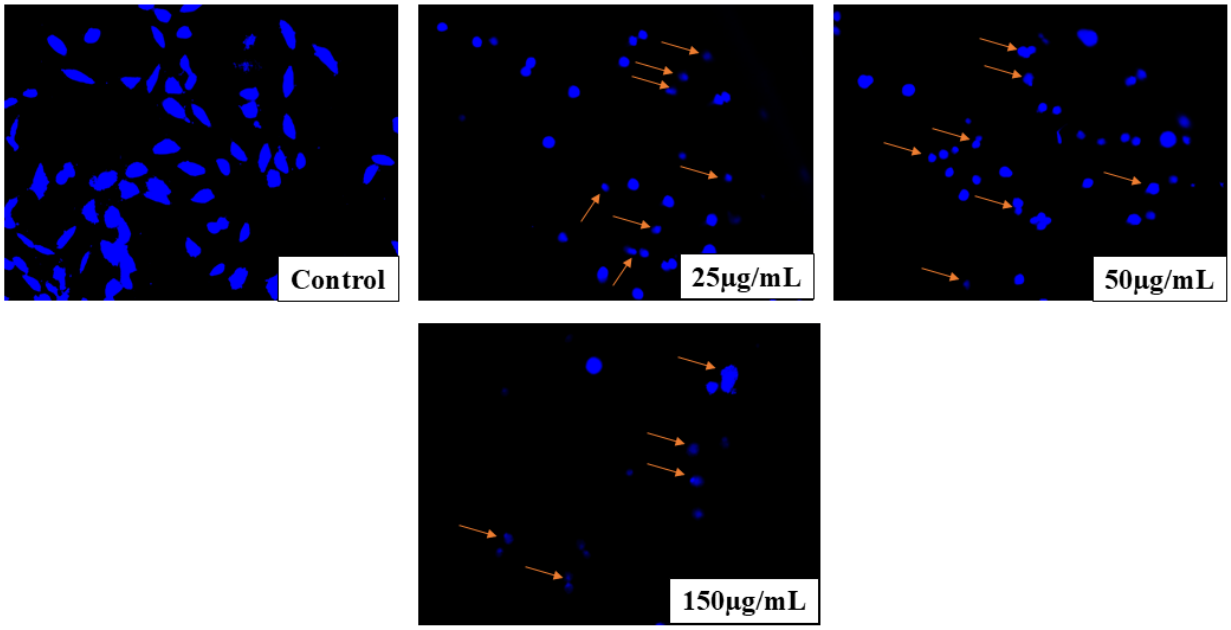

Figure 20. Morphological changes and nuclear fragmentation in A549 cells increase in proportion to the dose. The maximum deformities are observed at 150 µg/mL, confirming significant apoptosis.

3.9.4. Detection of apoptosis using PI staining.

PI dye specifically interacts with the dying/apoptotic cells, resulting in red colour fluorescence (late apoptotic/early necrotic phase cells stain red) [49]. Our investigation showed a noteworthy surge in the apoptotic cells as the level of BBG rose, as depicted in Figure 21, whereas in the control, no significant % apoptosis was observed.

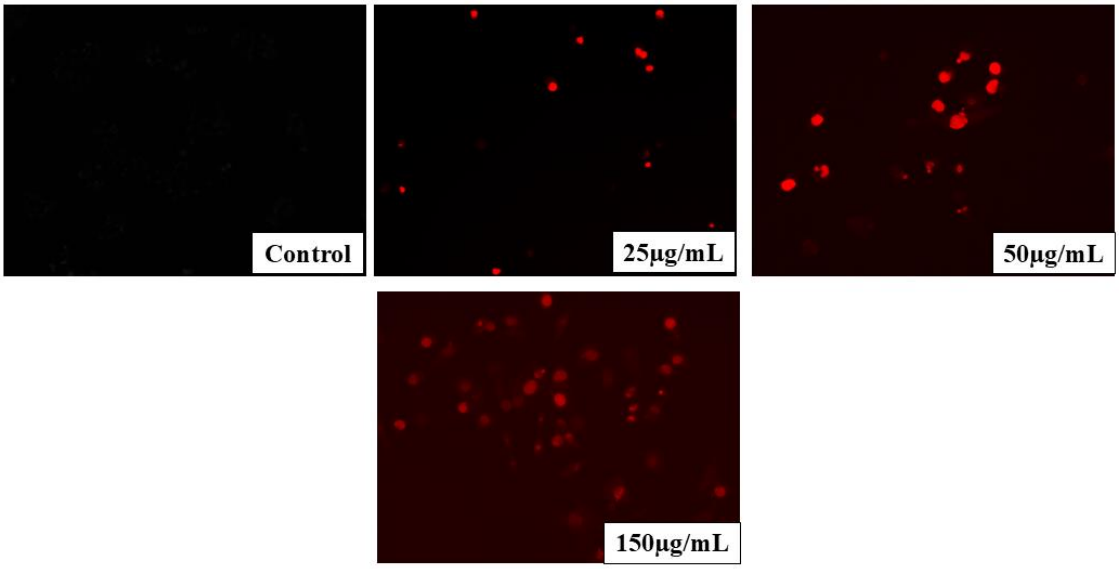

Figure 21. PI staining revealed increased fluorescence in A549 cells treated with BBG, indicating induction of apoptosis.

3.9.5. Hoechst and PI dual staining.

Hoechst/PI dual staining was executed to illustrate the nuclear morphology and apoptosis collectively. In our findings, the dead cells appeared pink/red, as depicted in Figure 22. We found that nuclear morphological variations and apoptosis increased in a dose-dependent manner.

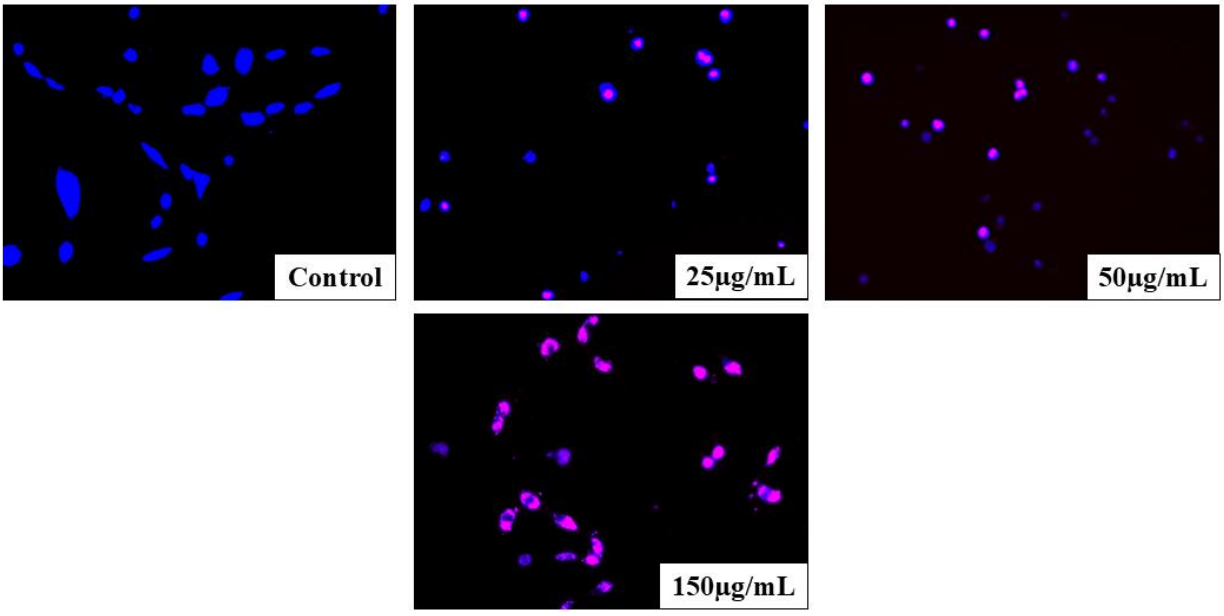

Figure 22. The absence of pink in control cells (blue only) confirmed their healthy state. The appearance of pink fluorescence in BBG-treated A549 cells indicated membrane disruption and DNA intercalation, confirming the onset of apoptosis.

3.9.6. Evaluation of Reactive oxygen species (ROS) generation.

ROS generation is an essential event in cells for maintaining regulatory metabolism. Free radical scavenging is present in our living system (in normal cells) to manage ROS generation and elimination, but in neoplastic cells to manage enhanced metabolic activities and the high levels of ROS produced [33,50]. In our findings, a significant increase in ROS generation was observed with increasing dose, as depicted in Figure 23.

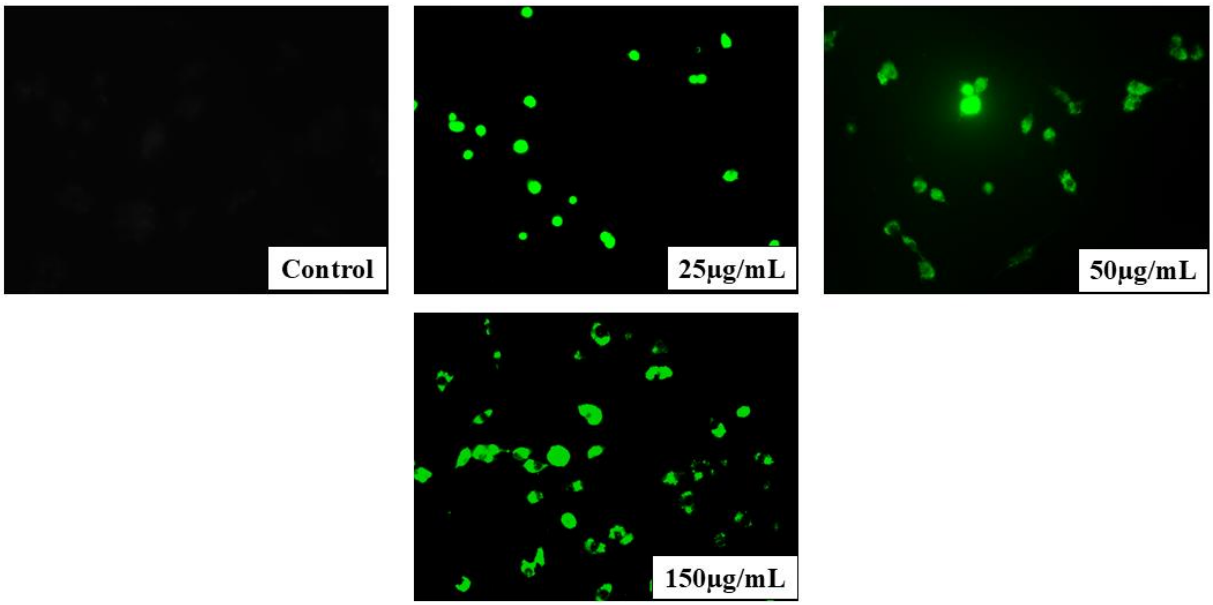

Figure 23. Intracellular ROS generation increases in proportion to dose, leading to cellular damage.

3.9.7. Acridine orange and ethidium bromide (AO/EtBr) staining for identifying cells in early and late apoptotic stages.

The AO/EtBr staining method is deemed immensely effective for detecting early & late apoptotic cells. EtBr is only accessible to the dead cells (Shows red fluorescence). However, AO exhibits permeability across all the cells (shows fluorescence in green color). Cells in the initial apoptotic phase exhibit a yellowish-orange hue, whereas those in the late-apoptotic phase display an orange-red color. In our findings, cells displayed yellow-orange-red coloration in early and late apoptosis, as depicted in Figure 24.

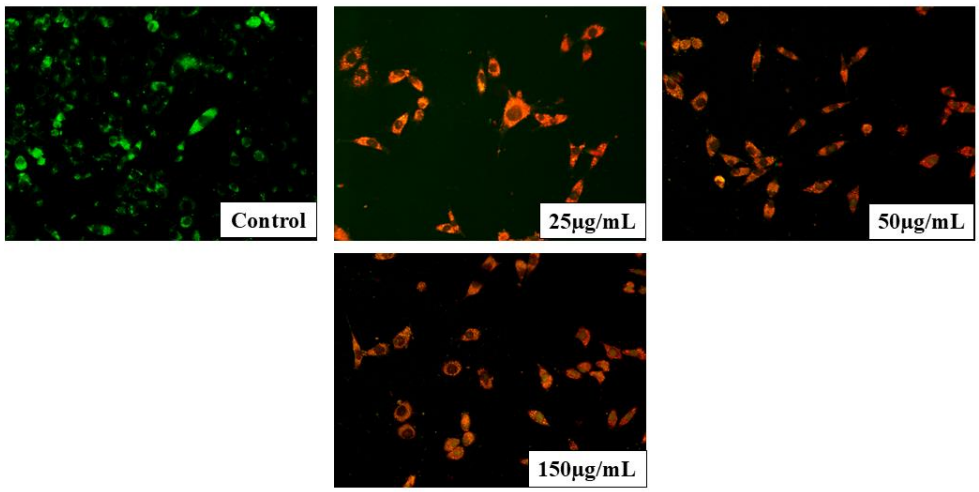

Figure 24. AO/EtBr staining of A549 cells, light yellowish cells indicate early apoptosis, while orange cells represent late-stage apoptosis.

3.10. Limitations and future direction.

Future research directions have been identified, including *in vivo* validation, pharmacokinetic and toxicity studies, and other mechanistic studies, to support the translational potential of BBG.

4. Conclusions

This study evaluated the pharmacokinetics of BG and its interaction with LC to assess its anticancer potential. We identified 95 common targets, with CDK1, ABCB1, and ADORA2A showing the strongest binding in molecular docking analysis. BBG significantly reduced A549 cell viability and proliferation at higher doses, with nuclear condensation, fragmentation, and apoptosis confirmed through Hoechst, PI, Hoechst/PI, and AO/EtBr staining. BBG was non-toxic to normal cells and induced ROS generation in A549 cells. Overall, the findings indicate that BBG exhibits notable anti-proliferative and antioxidant activity. The use of *in vitro* and *in silico* methods, which might not accurately reflect *in vivo* settings, limits the current work. To better determine therapeutic potential, safety, and pharmacokinetics, future research should focus on improved structural characterization, evaluation across multiple cancer and normal cell lines, mechanistic validation of predicted targets, and in vivo studies.

Author Contributions

Conceptualization, T.K.U.; methodology, T.K.U.; investigation, T.K.U.; validation, T.K.U. and A.A.; writing—original draft preparation, R.K., T.K.U. and A.A.; writing—review and editing, T.K.U. and A.A.; visualization, R.K.; supervision, T.K.U.; project administration, T.K.U. All authors have read and agreed to the published version of the manuscript.

Institutional Review Board Statement

Not applicable.

Informed Consent Statement

Not applicable.

Data Availability Statement

All data that support the findings of this research article will be available from the corresponding author upon request.

Funding

This work was supported by the Research and Development Cell, Parul University, Vadodara, Gujarat in the form of M.Sc. dissertation, PG contingency support, CR4D/IMSL/046.

Acknowledgments

The authors expressed their deep gratitude to Dr. Geetika Madan Patel, Medical Director and Vice President of the Research and Development Cell (RDC) at Parul University, Vadodara.

The authors also thanked the RDC team and the lab members of the Animal Cell Culture and Immunobiochemistry Lab for their valuable support.

Conflicts of Interest

The authors declare no conflict of interest.

Abbreviations

Abbreviation	Definition
AA	Ascorbic acid
BBG	Barley β-glucan
BG	Beta Glucan
LC	Lung cancer
PBS	Phosphate buffer saline
NSCLC	Non-small cell lung cancer
PPI	Protein-protein interaction
rxn	Reaction
DPPH	2,2-Diphenyl-1-picrylhydrazyl
FRAP	Ferric Reducing Antioxidant Power
ABTS	2,2'-azino-bis (3-ethylbenzothiazoline-6-sulfonic acid)
RPA	Reducing power assay
H_2O_2	Hydrogen peroxide
MTT	3-(4,5-dimethylthiazol-2-yl)-2,5-diphenyltetrazolium bromide
ROS	Reactive oxygen species
PI	Propidium iodide
H2DCFDA	2',7'-Dichlorodihydrofluorescein diacetate

References

1. Bray, F.; Laversanne, M.; Sung, H.; Ferlay, J.; Siegel, R.L.; Soerjomataram, I.; Jemal, A. Global cancer statistics 2022: GLOBOCAN estimates of incidence and mortality worldwide for 36 cancers in 185 countries. *CA Cancer J. Clin.* **2024**, *74*, 229-263, https://doi.org/10.3322/caac.21834.
2. Ross, P.; Farrell, M.P. The Road to Structurally Defined β-Glucans. *Chem. Rec.* **2021**, *21*, 3178–3193, https://doi.org/10.1002/tcr.202100059.
3. Bohn, J.A.; BeMiller, J.N. (1→3)-β-d-Glucans as biological response modifiers: a review of structure-functional activity relationships. *Carbohydr. Polym.* **1995**, *28*, 3–14, https://doi.org/10.1016/0144-8617(95)00076-3.
4. Lopez-Sanchez, P.; Wang, D.; Zhang, Z.; Flanagan, B.; Gidley, M.J. Microstructure and mechanical properties of arabinoxylan and (1,3;1,4)-β-glucan gels produced by cryo-gelation. *Carbohydr. Polym.* **2016**, *151*, 862–870, https://doi.org/10.1016/j.carbpol.2016.06.038.
5. Zhong, X.; Wang, G.; Li, F.; Fang, S.; Zhou, S.; Ishiwata, A.; Tonevitsky, A.G.; Shkurnikov, M.; Cai, H.; Ding, F. Immunomodulatory Effect and Biological Significance of β-Glucans. *Pharmaceutics* **2023**, *15*, 1615, https://doi.org/10.3390/pharmaceutics15061615.
6. Goudar, G.; Sharma, P.; Janghu, S.; Longvah, T. Effect of processing on barley β-glucan content, its molecular weight and extractability. *Int. J. Biol. Macromol.* **2020**, *162*, 1204-1216, https://doi.org/10.1016/j.ijbiomac.2020.06.208.
7. Wang, M.; Pan, J.; Xiang, W.; You, Z.; Zhang, Y.; Wang, J.; Zhang, A. β-glucan: a potent adjuvant in immunotherapy for digestive tract tumors. *Front. Immunol.* **2024**, *15*, 1424261, https://doi.org/10.3389/fimmu.2024.1424261.
8. Li, Q.; Lei, X.; Zhu, J.; Zhong, Y.; Yang, J.; Wang, J.; Tan, H. Radiotherapy/Chemotherapy-Immunotherapy for Cancer Management: From Mechanisms to Clinical Implications. *Oxid. Med. Cell. Longev.* **2023**, *2023*, 7530794, https://doi.org/10.1155/2023/7530794.
9. Brown, G.D.; Gordon, S. A new receptor for β-glucans. *Nature* **2001**, *413*, 36–37, https://doi.org/10.1038/35092620.
10. Sletmoen, M.; Stokke, B.T. Higher order structure of (1,3)-β-D-glucans and its influence on their biological activities and complexation abilities. *Biopolymers* **2008**, *89*, 310–321, https://doi.org/10.1002/bip.20920.

11. Chan, G.C.-F.; Chan, W.K.; Sze, D.M.-Y. The effects of β-glucan on human immune and cancer cells. *J. Hematol. Oncol.* **2009**, *2*, 25, https://doi.org/10.1186/1756-8722-2-25.
12. Taylor, P.R.; Tsoni, S.V.; Willment, J.A.; Dennehy, K.M.; Rosas, M.; Findon, H.; Haynes, K.; Steele, C.; Botto, M.; Gordon, S.; Brown, G.D. Dectin-1 is required for β-glucan recognition and control of fungal infection. *Nat. Immunol.* **2007**, *8*, 31-38, https://doi.org/10.1038/ni1408.
13. Pires, D.E.V.; Blundell, T.L.; Ascher, D.B. pkCSM: Predicting Small-Molecule Pharmacokinetic and Toxicity Properties Using Graph-Based Signatures. *J. Med. Chem.* **2015**, *58*, 4066-4072, https://doi.org/10.1021/acs.jmedchem.5b00104.
14. Daina, A.; Michielin, O.; Zoete, V. SwissADME: a free web tool to evaluate pharmacokinetics, drug-likeness and medicinal chemistry friendliness of small molecules. *Sci. Rep.* **2017**, *7*, 42717, https://doi.org/10.1038/srep42717.
15. Banerjee, P.; Kemmler, E.; Dunkel, M.; Preissner, R. ProTox 3.0: a webserver for the prediction of toxicity of chemicals. *Nucleic Acids Res.* **2024**, *52*, W513–W520, https://doi.org/10.1093/nar/gkae303.
16. Sihombing, I.N.N.; Arsianti, A. Network pharmacology prediction and molecular docking analysis on the mechanism of eugenol as a candidate against estrogen receptor-positive breast cancer. *J. Pharm. Pharmacogn. Res.* **2024**, *12*, 837–851.
17. Lee, K.; Choi, Y.-J.; Lim, H.-I.; Cho, K.J.; Kang, N.; Ko, S.-G. Network pharmacology study to explore the multiple molecular mechanism of SH003 in the treatment of non-small cell lung cancer. *BMC Complement. Med. Ther.* **2024**, *24*, 70, https://doi.org/10.1186/s12906-024-04347-y.
18. Stelzer, G.; Rosen, N.; Plaschkes, I.; Zimmerman, S.; Twik, M.; Fishilevich, S.; Stein, T.I.; Nudel, R.; Lieder, I.; Mazor, Y.; Kaplan, S.; Dahary, D.; Warshawsky, D.; Guan-Golan, Y.; Kohn, A.; Rappaport, N.; Safran, M.; Lancet, D. The GeneCards Suite: From Gene Data Mining to Disease Genome Sequence Analyses. *Curr. Protoc. Bioinform.* **2016**, *54*, 1.30.31-31.30.33, https://doi.org/10.1002/cpbi.5.
19. Szklarczyk, D.; Kirsch, R.; Koutrouli, M.; Nastou, K.; Mehryary, F.; Hachilif, R.; Gable, A.L.; Fang, T.; Doncheva, Nadezhda T.; Pyysalo, S.; Bork, P.; Jensen, Lars J.; von Mering, C. The STRING database in 2023: protein–protein association networks and functional enrichment analyses for any sequenced genome of interest. *Nucleic Acids Res.* **2023**, *51*, D638-D646, https://doi.org/10.1093/nar/gkac1000.
20. Shannon, P.; Markiel, A.; Ozier, O.; Baliga, N.S.; Wang, J.T.; Ramage, D.; Amin, N.; Schwikowski, B.; Ideker, T. Cytoscape: A Software Environment for Integrated Models of Biomolecular Interaction Networks. *Genome Res.* **2003**, *13*, 2498-2504, https://doi.org/10.1101/gr.1239303.
21. Burley, S.K.; Bhikadiya, C.; Bi, C.; Bittrich, S.; Chao, H.; Chen, L.; Craig, P.A.; Crichlow, G.V.; Dalenberg, K.; Duarte, J.M.; Dutta, S.; Fayazi, M.; Feng, Z.; Flatt, J.W.; Ganesan, S.; Ghosh, S.; Goodsell, D.S.; Green, R.K.; Guranovic, V.; Henry, J.; Hudson, B.P.; Khokhriakov, I.; Lawson, C.L.; Liang, Y.; Lowe, R.; Peisach, E.; Persikova, I.; Piehl, D.W.; Rose, Y.; Sali, A.; Segura, J.; Sekharan, M.; Shao, C.; Vallat, B.; Voigt, M.; Webb, B.; Westbrook, J.D.; Whetstone, S.; Young, J.Y.; Zalevsky, A.; Zardecki, C. RCSB Protein Data Bank (RCSB.org): delivery of experimentally-determined PDB structures alongside one million computed structure models of proteins from artificial intelligence/machine learning. *Nucleic Acids Res.* **2023**, *51*, D488-D508, https://doi.org/10.1093/nar/gkac1077.
22. Tian, W.; Chen, C.; Lei, X.; Zhao, J.; Liang, J. CASTp 3.0: computed atlas of surface topography of proteins. *Nucleic Acids Res.* **2018**, *46*, W363-W367, https://doi.org/10.1093/nar/gky473.
23. Hossain, S.; Sarkar, B.; Prottoy, M.N.I.; Araf, Y.; Taniya, M.A.; Ullah, M.A. Thrombolytic Activity, Drug Likeness Property and ADME/T Analysis of Isolated Phytochemicals from Ginger (*Zingiber officinale*) Using *In silico* Approaches. *Mod. Res. Inflamm.* **2019**, *8*, 29-43, https://doi.org/10.4236/mri.2019.83003.
24. Ahmad, A.; Anjum, F.M.; Zahoor, T.; Chatha, Z.A.; Nawaz, H. EFFECT OF BARLEY β-GLUCAN ON SENSORY CHARACTERISTICS OF BREAD. *Pak. J. Agri. Sci.* **2008**, *45*, 88-94.
25. Richards, C.; O'Connor, N.; Jose, D.; Barrett, A.; Regan, F. Selection and optimization of protein and carbohydrate assays for the characterization of marine biofouling. *Anal. Methods* **2020**, *12*, 2228-2236, https://doi.org/10.1039/D0AY00272K.
26. Gründemann, C.; Garcia-Käufer, M.; Sauer, B.; Scheer, R.; Merdivan, S.; Bettin, P.; Huber, R.; Lindequist, U. Comparative chemical and biological investigations of β-glucan-containing products from shiitake mushrooms. *J. Funct. Foods* **2015**, *18*, 692-702, https://doi.org/10.1016/j.jff.2015.08.022.
27. Sahoo, M.R.; Umashankara, M.S. FTIR Based Metabolomics Profiling and Fingerprinting of Some Medicinal Plants: An Attempt to Develop an Approach for Quality Control and Standardization of Herbal Materials. *Pharmacogn. Res.* **2022**, *15*, 163–167.

28. Chen, L.; Cui, C.; Wang, Z.; Che, F.; Chen, Z.; Feng, S. Structural Characterization and Antioxidant Activity of β-Glucans from Highland Barley Obtained with Ultrasonic–Microwave-Assisted Extraction. *Molecules* **2024**, *29*, 684, https://doi.org/10.3390/molecules29030684.
29. Trivedi, R.; Upadhyay, T.K. Preparation, characterization and antioxidant and anticancerous potential of Quercetin loaded β-glucan particles derived from mushroom and yeast. *Sci. Rep.* **2024**, *14*, 16047, https://doi.org/10.1038/s41598-024-66824-1.
30. Kiani, R.; Arzani, A.; Mirmohammady Maibody, S.A.M. Polyphenols, Flavonoids, and Antioxidant Activity Involved in Salt Tolerance in Wheat, *Aegilops cylindrica* and Their Amphidiploids. *Front. Plant Sci.* **2021**, *12*, 646221, https://doi.org/10.3389/fpls.2021.646221.
31. Ebrahimi, F.; Subbiah, V.; Agar, O.T.; Bringloe, T.T.; Legione, A.R.; Suleria, H.A.R. LC-ESI-QTOF-MS/MS characterization of phenolic compounds from Victorian shorebound red seaweeds and their antioxidant capacity. *Algal Res.* **2024**, *82*, 103609, https://doi.org/10.1016/j.algal.2024.103609.
32. Kini, R.; Trivedi, R.; Mujahid, M.H.; Patra, P.; Alharbi, S.A.; Alshammari, F.D.; Bealy, M.B.; Elkhalifa, A.E.O.; Siddiqui, S.; Upadhyay, T.K. Green Synthesis and Characterization of Silver Nanoparticles from Nerium indicum and Investigation of Antioxidant and Anti-Cancerous Potential against Cervical Cancer Cell Line (HeLa). *Ind. J. Pharm. Educ. Res* **2024**, *58*, 565-578, https://doi.org/10.5530/ijper.58.2.63.
33. Upadhyay, T.K.; Trivedi, R.; Khan, F.; Al-Keridis, L.A.; Pandey, P.; Sharangi, A.B.; Alshammari, N.; Abdullah, N.M.; Yadav, D.K.; Saeed, M. *In vitro* elucidation of antioxidant, antiproliferative, and apoptotic potential of yeast-derived β-1,3-glucan particles against cervical cancer cells. *Front. Oncol.* **2022**, *12*, 942075, https://doi.org/10.3389/fonc.2022.942075.
34. Feng, X.; Shang, J.; Wang, Y.; Chen, Y.; Liu, Y. Exploring the Properties and Application Potential of β-Glucan in Skin Care. *Food Sci. Nutr.* **2025**, *13*, e70212, https://doi.org/10.1002/fsn3.70212.
35. Alsedfy, M.Y.; Ebnalwaled, A.A.; Moustafa, M.; Said, A.H. Investigating the binding affinity, molecular dynamics, and ADMET properties of curcumin-IONPs as a mucoadhesive bioavailable oral treatment for iron deficiency anemia. *Sci. Rep.* **2024**, *14*, 22027, https://doi.org/10.1038/s41598-024-72577-8.
36. Widyananda, M.H.; Pratama, S.K.; Samoedra, R.S.; Sari, F.N.; Kharisma, V.D.; Ansori, A.N.M.; Antonius, Y. Molecular docking study of sea urchin (*Arbacia lixula*) peptides as multi-target inhibitor for non-small cell lung cancer (NSCLC) associated proteins. *J. Pharm. Pharmacogn. Res.* **2021**, *9*, 484-496.
37. Massacci, G.; Perfetto, L.; Sacco, F. The Cyclin-dependent kinase 1: more than a cell cycle regulator. *Br. J. Cancer* **2023**, *129*, 1707–1716, https://doi.org/10.1038/s41416-023-02468-8.
38. Wang, Q.; Bode, A.M.; Zhang, T. Targeting CDK1 in cancer: mechanisms and implications. *Npj Precis. Oncol.* **2023**, *7*, 58, https://doi.org/10.1038/s41698-023-00407-7.
39. Pellarin, I.; Dall'Acqua, A.; Favero, A.; Segatto, I.; Rossi, V.; Crestan, N.; Karimbayli, J.; Belletti, B.; Baldassarre, G. Cyclin-dependent protein kinases and cell cycle regulation in biology and disease. *Signal Transduct Target Ther.* **2025**, *10*, 11, https://doi.org/10.1038/s41392-024-02080-z.
40. Skinner, K.T.; Palkar, A.M.; Hong, A.L. Genetics of *ABCB1* in Cancer. *Cancers* **2023**, *15*, 4236, https://doi.org/10.3390/cancers15174236.
41. Shreenivas, A.; Nishizaki, D.; Lee, S.; Pabla, S.; Nesline, M.; Conroy, J.M.; DePietro, P.; Kato, S.; Kurzrock, R. Clinical and Biologic Correlates of ADORA2A Transcriptomic Expression in Cancer. *Int. J. Mol. Sci.* **2024**, *25*, 4742, https://doi.org/10.3390/ijms25094742.
42. Özen, S.; Ünlü, A.; Özbek, H.N.; Göğüş, F. β-Glucan Extraction from Hull-Less Barley by a Novel Approach: Microwave-Assisted Pressurized CO_2/H_2O. *Food Bioprocess Technol.* **2024**, *17*, 4781–4793, https://doi.org/10.1007/s11947-024-03420-1.
43. Shah, A.; Ahmad, M.; Ashwar, B.A.; Gani, A.; Masoodi, F.A.; Wani, I.A.; Wani, S.M.; Gani, A. Effect of γ-irradiation on structure and nutraceutical potential of β-d-glucan from barley (*Hordeum vulgare*). *Int. J. Biol. Macromol.* **2015**, *72*, 1168-1175, https://doi.org/10.1016/j.ijbiomac.2014.08.056.
44. Chioru, A.; Chirsanova, A.; Dabija, A.; Avrămia, I.; Boiștean, A.; Chetrariu, A. Extraction Methods and Characterization of β-Glucans from Yeast Lees of Wines Produced Using Different Technologies. *Foods* **2024**, *13*, 3982, https://doi.org/10.3390/foods13243982.
45. Irshad, M.; Zafaryab, M.; Singh, M.; Rizvi, M.M.A. Comparative Analysis of the Antioxidant Activity of *Cassia fistula* Extracts. *Int. J. Med. Chem.* **2012**, *2012*, 157125, https://doi.org/10.1155/2012/157125.
46. Rutckeviski, R.; Corso, C.R.; Fonseca, A.S.; Rodrigues, M.L.; Román-Ochoa, Y.; Cipriani, T.R.; Cavalli, L.R.; Cadena, S.M.S.C.; Smiderle, F.R. Anti-Cancer Potential of Linear β-(1→6)-D-Glucan from *Agaricus bisporus* on Estrogen Receptor-Positive (ER+) Breast Cancer Cells. *Molecules* **2024**, *29*, 4781, https://doi.org/10.3390/molecules29194781.

47. Joha, Z.; Ergül, M. Unraveling the Role of Apoptosis in the Antiproliferative Activity of β-Glucan on A549 Cells. *Cumhur. Sci. J.* **2023**, *44*, 640–644, https://doi.org/10.17776/csj.1336167.
48. Hart, M.C.; Isuri, R.K.; Ramos, D.; Osharovich, S.A.; Rodriguez, A.E.; Harmsen, S.; Dudek, G.C.; Huck, J.L.; Holt, D.E.; Popov, A.V.; Singhal, S.; Delikatny, E.J. Non-Small Cell Lung Cancer Imaging Using a Phospholipase A2 Activatable Fluorophore. *Chem. Biomed. Imaging* **2024**, *2*, 490-500, https://doi.org/10.1021/cbmi.4c00026.
49. Krapoth, T.C.; Henle, G.S.; Avdyli, M.; Bektić, B.; Schwarzkopf, K.M.; Bešić, L.; Zeuzem, S.; Welsch, C.; Kraus, N.; Ortiz, C. Wanted: Dead or Alive Cells with Propidium Iodide Staining in Liver Tissue. *Int. J. Mol. Sci.* **2024**, *25*, 13521, https://doi.org/10.3390/ijms252413521.
50. Verma, P.; Rishi, B.; George, N.G.; Kushwaha, N.; Dhandha, H.; Kaur, M.; Jain, A.; Jain, A.; Chaudhry, S.; Singh, A.; Siraj, F.; Misra, A. Recent advances and future directions in etiopathogenesis and mechanisms of reactive oxygen species in cancer treatment. *Pathol. Oncol. Res.* **2023**, *29*, 1611415, https://doi.org/10.3389/pore.2023.1611415.

Publisher's Note & Disclaimer